34th Annual International Conference of the IEEE EMBS
San Diego, California USA, 28 August - 1 September, 2012

Automated material map generation from MRI scout pairs for preclinical PET attenuation correction

Peter Bandi, Norbert Zsoter, Peter Koncz, Magor Babos, Sandor Hobor, Domokos Mathe, Laszlo Papp

***Abstract*— A novel method is presented to perform material map segmentation from preclinical MRI for corresponding PET attenuation correction. MRI does not provide attenuation ratio, hence segmenting a material map from it is challenging. Furthermore the MRI images often suffer from ghost artifacts. On the contrary MRI has no radiation dose. Our method operated with fast spin echo scout pairs that had perpendicular frequency directions. This way the direction of the ghost artifacts were perpendicular as well. Our body-air segmentation method built on this a priori information and successfully erased the ghost artifacts from the final binary mask. Visual and quantitative validation was performed by two preclinical specialists. Results indicate that our method is effective against MRI scout ghost artifacts and that PET attenuation correction based on MRI makes sense even on preclinical images.**

I. INTRODUCTION

By the perspective of biochemical and pharmaceutical research, rodent experiments are excellent alternatives to human experiments [1]. Although, metabolic events are quite similar in both species, extreme size differences require special preclinical medical cameras. In the field of preclinical oncological research, PET-CT is a widely used multi-modal solution [2]. While PET provides functional information of metabolic events, CT provides anatomical and structural information and it is a good base of PET attenuation correction (AC) [3]. It is a common knowledge that CT is an undue radiation source for the living body and it has a poor soft tissue contrast. In case of preclinical studies one often decides to acquire several CT scans in a row [4]. This method significantly increases the radiation dose of the rodent which ultimately affects the tumor healing. Recent papers indicate that this ratio of the dose coming from the CT is approx. 35-40% of the overall radiation dose [5]. Due to this reason the acquisition itself may modify the results of the experiment.

MRI as an upcoming modality may be an alternative of CT, since it has no known negative effect to the living body and has an excellent soft tissue contrast ratio (see Fig. 1). In return it is more challenging to acquire material maps for PET attenuation correction from MRI, since it does not provide attenuation ratio [6], [7] as CT does. Furthermore, an MRI scan takes more time than a CT scan does. Therefore MRI scans are mostly acquired only from the important parts of the body, however PET examinations usually cover the whole body. Since acquiring a whole body multi-FOV MRI scan is very time-consuming (approx. 15-20 min/FOV), fast MRI scout scans are acquired for localization (approx. 4 min/FOV). Scout images have a moderate resolution, and they have ghost artifacts perpendicular to the actual frequency direction directly connecting to body regions (see Fig. 2). These artifacts are generated by respiratory movements and fluid motion inside of the bowel [8]. The voxel value of these artifacts is quite similar to the values of the body, hence the proper way of their segmentation from a single images is not trivial at all. In spite of these facts it seems logical to use these fast scout scans for PET attenuation correction, since these scans cover the whole body. Our assumption was that acquiring two fast gradient echo scout images about the same region having perpendicular frequency directions could aid us to develop a segmentation method to accurately deal with ghost artifacts (see Fig. 2). Building on the above a priori knowledge, we performed multiple variable analyses to generate the final body-air mask. Since rodents have much smaller size than humans have, the effect of attenuation is not so significant than in a human body. The latter case generally requires material maps having bone, lung, soft tissue and air indices [9]. On the contrary a body-air mask may be already sufficient for preclinical PET attenuation corrections.

P. Bandi, N. Zsoter P. Koncz, M. Babos, S. Hobor and L. Papp are with Mediso Medical Imaging Systems Ltd., Baross str. 91-95, H-1047 Budapest, Hungary, peter.bandi@mediso.hu

M. Domokos is with CROmed Research Ltd, Baross str. 91-95, H-1047 Budapest, Hungary

II. MATERIALS AND METHODS

A. Patient images

We collected 12 3D steady-state gradient echo MRI scout pair sequences and the corresponding PET acquisition data acquired by nanoScan PM PET/MRI preclinical camera system developed by Mediso. All MRI scout sequences were multi-FOV acquisitions. One FOV took 4 minutes with 6cm/FOV coverage. The number of FOVs were 2-5 per study. The reconstructed MRI sequences had 0.46x0.46mm axial resolution, and the pixel spacing between slices was 0.5mm.

B. Methods

Let us denote the set of all three-dimensional volumes by $\mathcal{V} = \left\{[v_{ijk}]_{mno}\right\}^*$ expression, where m, n, o respectively mean the axial, sagittal and coronal size of the given volume. Based on this definition let us denote the MRI scout pairs as $MR_1 \in \mathcal{V}$ and $MR_2 \in \mathcal{V}$ respectively. Let us assume that the expression $v = I(\bar{c})$ means that the value of $I \in \mathcal{V}$ at index $\bar{c} \in \mathbb{N}^3$ is $v \in \mathbb{R}$. We assumed that $(c_1, c_2, c_3) = \bar{c}$ values represented indexing in axial, sagittal and coronal directions respectively. We denoted the set of all valid index coordinates of an $I \in \mathcal{V}$ image by C_I

978-1-4577-1787-1/12/$26.00 ©2012 IEEE

1) Noise reduction: 3D Gaussian smoothing was performed over the MRI axial slices with 0.46 deviation and $5 \times 5 \times 5$ pixels kernel size [10]. The smoothed images were denoted by $MR_1^s \in \mathcal{V}$ and $MR_2^s \in \mathcal{V}$ respectively.

2) Region growing from background: Our method took samples from the background region of our MRI images for image specific statistical analyses. The reason why we did not use simple thresholds was that finding such an optimal threshold value was not trivial at all in case of MRI images. Even histogram based threshold could not be determined, since the MRI images - partly because of Rayleigh distribution - rarely have separated peaks on their histogram [6], [7].

We modified our MRI acquisitions to always have 3 axial slices at the beginning of our images containing no body parts, only air. We used these slices to determine the parameters of the background noise Rayleigh distribution [6], [7]. The indices of necessary voxel values that served as the base of the statistical measurement were collected into $R_1 \subset \left\{\bar{i} \in \mathbb{N}^3\right\}$ and $R_2 \subset \left\{\bar{j} \in \mathbb{N}^3\right\}$ sets by an operator defined as eq. 1.

$$f_{bck}(a,b) : \forall \bar{c} \in V_{MR_i} | a \leq c_1 \leq b : R_i \cup \bar{c} \qquad (1)$$

where $i = 1, 2$ and $a = 1, b = 3$.

Since the distribution of values in MR_1^s and MR_2^s taken from those coordinates being inside of R_1 and R_2 was Rayleigh, we calculated the $\hat{\sigma}$ maximum likelihood estimate of σ mode for both value sets by eq. 2.

$$\hat{\sigma}_i = \sqrt{\frac{1}{2 * |R_i|} \sum_{v=MR_i^s(\bar{c} \in R_i)} v^2} \qquad (2)$$

where $i = 1, 2$

We determined $m_1 \in \mathbb{R}$ and $m_2 \in \mathbb{R}$ values for MR_1^s and MR_2^s respectively were background voxel values were under m_1 and m_2 with $p \in \mathbb{R}$ probability. We calculated m_1 and m_2 by using the cumulative distribution function [11] as defined by eq. 3.

$$F(m_i) = 1 - e^{-\frac{m_i^2}{2\hat{\sigma}_i^2}} = p \qquad (3)$$

where $i = 1, 2$

Based on initial trials, $p = 0.95$ was an appropriate choice in our cases. Solving these equations gave us m_1 and m_2 values. Based on these values - and the above general term of the background noise distribution - our method performed a recursive region growing from a background position in both MR_1^s and MR_2^s images independently. The $\bar{s}_1 \in \mathbb{N}^3$ and $\bar{s}_2 \in \mathbb{N}^3$ seed points of the region grow were the geometric centers of those coordinates collected into R_1 and R_2 sets respectively. During the region grows performed in MR_1^s and MR_2^s independently we recursively checked the 6 neighbors of a given coordinate. We referred to the coordinate set of 6 neighbors of a $\bar{c} \in \mathbb{N}^3$ as $N_{\bar{c}}$ where $|N_{\bar{c}}| = 6$.

The noise reduction step detailed in sec. II-B.1 slightly changed (depressed) the background noise distribution, but this way our region growing operated with a higher accuracy. The result of both region growing were stored in binary masks where background and body points had false and true values respectively. We denoted these masks as $MR_1^b \in \mathcal{V}$ and $MR_2^b \in \mathcal{V}$.

TABLE I
ALGORITHMIC STEPS OF THE MRI BACKGROUND REGION GROWING

1	$Q \subset \left\{\mathbb{N}^3\right\}^*, Q = \oslash$
2	$Q \cup \bar{s}_i$
3	$MR_i^b(\bar{s}_i) = 1$
4	while $\|Q\| > 0$
5	if $\bar{c} \in Q$
6	$Q \setminus \bar{c}$
7	$\forall \bar{n} \in N_{\bar{c}}$
8	if $MR_i^b(\bar{n}) = 0$
9	if $MR_i^s(\bar{n}) \leq m_i$
10	$MR_i^b(\bar{n}) = 1$
11	$Q \cup \bar{n}$

where $i = 1, 2$

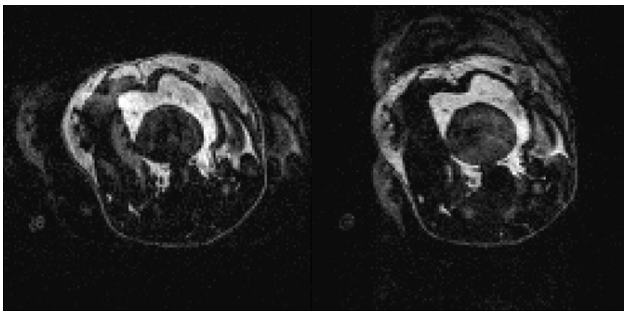

Fig. 2. Axial slices of corresponding MRI scout pairs representing ghost artifacts in perpendicular direction.

For the detailed steps of the region growing algorithm see Tab. I.

3) Registration of MRI image pairs: Since we wanted to simulate real daily routine, we did not wait for MRI coil heat-up, because we needed fast MRI scout scans to minimize the overall acquisition time. Hence the coil temperature during the MRI scout pair acquisitions was different. This resulted slight shift differences between the reconstructed MRI pairs. In order to resolve this issue we performed an automated rigid registration between MR_1^s and MR_2^s. The chosen similarity measurement was the Sum of Squared Differences (SSD) [12]. The similarity was measured only in those common coordinates where both MR_1^b and MR_2^b were true. This way the speed and the accuracy of the registration could be increased, since background regions were excluded. The sampling density was two times of the voxel sizes in all directions. To optimize the SSD measurement, we used the Nelder-Mead method [13], [14]. The reference of the registration was the MR_1^s image. The result of current step was a $T \in \mathbb{R}^3$ translation.

4) Common mask generation: Having the T translation between MR_1^s and MR_2^s provided by the previous step led us to an optimal fit on the image pairs. Based on this translation

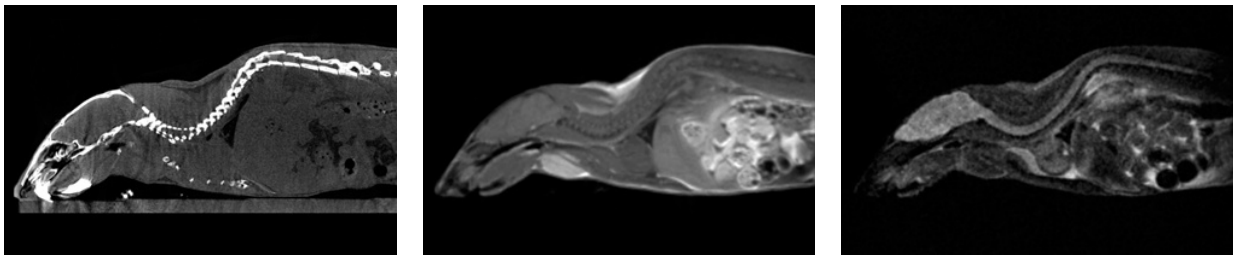

Fig. 1. Left: Sagittal CT plane of a rat. Middle: sagittal T1 MRI plane of the same rat. Right: sagittal T2 MRI plane of the same rat. Note the soft tissue contrast ratio of MRI images comparing to the CT and that bones are not present on MRI images.

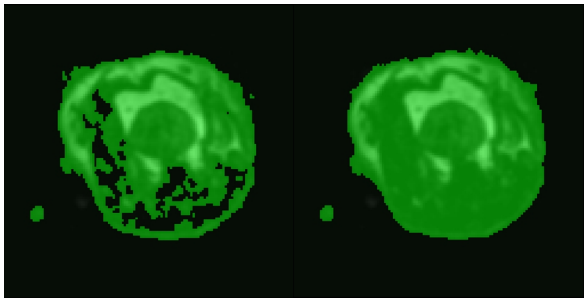

Fig. 3. Left: Axial view of an MRI fused with its corresponding common mask having holes inside. Right: The same axial view representing the corrected, filled common mask with the same MRI. Note that the small bottom-left mask spot covers the intersection of the slice with the tail.

MR_1^b and MR_2^b were superimposed. The registered MR_2^b was denoted by $T(MR_2^b)$. A logical AND operator was applied on spatially overlapping voxels between MR_1^b and $T(MR_2^b)$ to generate a $MR^b \in \mathcal{V}$ intersected mask (see Fig. 3).

5) Gap filling: Morphological dilation was performed on MR^b inside of a $3 \times 3 \times 3$ voxel sized kernel by considering the 6 neighbors of all true valued voxels. According to initial trials the above kernel configuration removed the gaps from our mask images. A three-dimensional region labeling was performed on the dilated MR^b [15], and the result was stored in $MR^l \in \mathcal{V}$. This way the internal and external air regions were separated. If a region volume inside of MR^l was less than 0.1 percent of the total image volume, it was classified as body region. Finally a morphological erosion was performed on the gap filled MR^l - as the opposite of the first dilation to preserve the correct volume of the body mask. The final mask was denoted by $MR^e \in \mathcal{V}$ (see Fig. 3).

C. Validation

Two preclinical specialists checked the accuracy of our binary body-air mask generation algorithm by visual inspection. They validated our method by examining the fused binary mask with one of the MRI scouts (see Fig. 3) and the NAC PET (see Fig. 4) of all 12 studies. Scoring of the segmentation was performed on a scale of 1 - 5 (1: worst, 5: best).

In order to validate the effect of our binary mask on the PET AC on both visual and quantitative level, a 237g

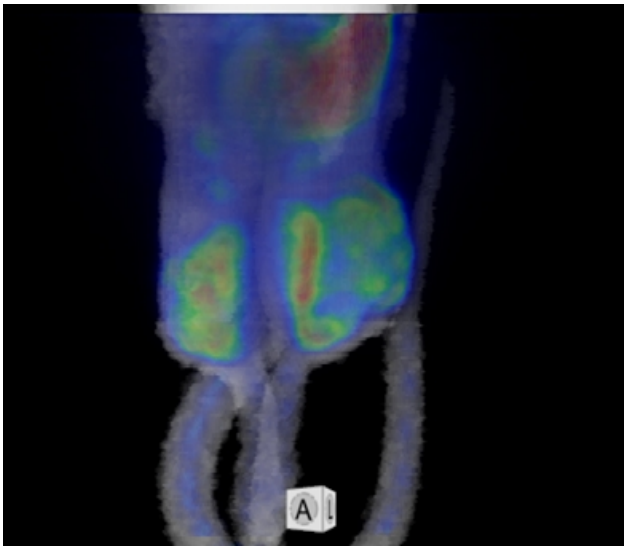

Fig. 4. Three-dimensional volume rendering (VR) view of the fused NAC PET and the final body-air mask derived from the corresponding MRI scout pair.

weighted Wistar rat was also involved into our validation, where a glioblastoma cell line tumor was placed in both flanks. FDG PET acquisition was performed 1 hour after injecting 10 MBq FDG.

Next to the MRI scout pairs, an additional multi-FOV T2 weighted MRI was acquired as well to aid the final visual analysis of the AC and non-AC PET images (see Fig. 5). The T2 image acquisition took 40 minutes. AC and non-AC PET image pairs were reconstructed with TeraTomo PET reconstruction engine [16]. The voxel size of the reconstructed PET was uniformly 0.4mm.

The specialists compared the AC and non-AC PET images fused with the T2 weighted MRI in Interview Fusion preclinical evaluation software. The comparison was done in two ways: visually and quantitatively. Latter one was done by placing two 3D isocount VOIs over two findings located inside of the legs.

III. RESULTS

A. Visual inspection

Overall 1 case got a score of 3 where the ghost effect was so high that even humans could not determine the exact

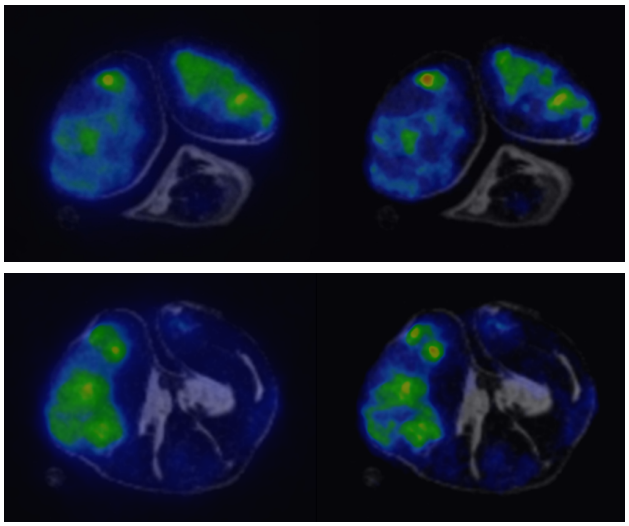

Fig. 5. A Wistar rat study. Left column: Different slices of a fused NAC PET-MRI fusion. Right: the corresponding fused slices of the AC PET with the same MRI. Note the sharper regions of hot spots on the AC PET.

boundary of the rat. 3 cases got score 4 where partial noises on the surface of the skin was present, although, these little noises did not affect the result or the PET reconstruction noticeably. All other cases got score 5. For axial slices of the Wistar rat representing NAC PET-MRI and AC PET-MRI fusion, see Fig. 5.

B. Quantitative analysis

According to the distribution of the cancer uptake, AC PET regions shown significantly higher uptake and better contrast ratio comparing to NAC PET images. The standard deviation of the AC PET regions shown average 7 - 21% higher values. Mean values were 32-63% higher in case of AC PET regions comparing to corresponding NAC PET regions.

IV. CONCLUSIONS AND FUTURE WORKS

A. Conclusions

We have proposed an automated method to generate an MRI based binary material map for PET attenuation correction. We built on the presence of MRI scout image pairs having perpendicular frequency directions to reduce the effect of ghost artifacts. According to the feedback of preclinical researchers the overall time to acquire the scout pairs is fairly acceptable comparing to time-consuming T1 and T2 acquisitions. Current results indicate that the method is effective against the above artifacts and required no human intervention. The statistical as well as the visual analysis proves that body-air based binary material maps bring great benefit in the process of PET reconstruction.

B. Future Works

We will focus on the segmentation of lungs which are normally differentiated from air in case of human examinations. Performing such a segmentation on our MRI scout pairs seems to be logical and feasible, since lungs - as the two largest air holes inside of our body-air mask - are present on our binary image with moderately noisy boundaries. Post-processing these internal holes could lead us to an acceptable lung segmentation. A three valued body-air-lung material map might bring benefits to the PET reconstruction when lung nodules are subject of the research. Generating a four valued material map including bones as well are currently beyond our scope, since bones can hardly be detected by MRI [17]. According to our current knowledge, bone segmentation form MRI could be achieved by atlas registration techniques [13].

V. ACKNOWLEDGEMENT

The research leading to these results has received funding from the European Union's Seventh Framework Programme (FP7/2007-2013) under grant agreement n° HEALTH-F2-2011-278850 (INMiND).

REFERENCES

[1] V. Koo, P. W. Hamilton, K. Williamson, Non-invasive in vivo imaging in small animal research, *Cell Oncol*, vol. 28, 2006, pp. 127-139.
[2] S. R. Cherry, Mutimodality Imaging: Beyond PET/CT and SPECT/CT, *Semin Nucl Med*, vol. 39, 2009, pp. 348 - 353.
[3] T. Beyer, D. W. Townsend, T. Brun, et al., A Combined PET/CT Scanner for Clinical Oncology, *J Nucl Med*, vol. 41, 2000, pp. 1369-1379.
[4] I. Willekens, N. Buls, T. Lahoutte, et al., Evaluation of the radiation dose in micro-CT with optimization of the scan protocol, *Contrast Media Mol Imaging*, vol. 5, 2010, pp. 201 - 2-7.
[5] S. K. Carlson, K. L. Classic, C. E. Bender, et al., Small Animal Absorbed Radiation Dose from Serial Micro-Computed Tomography Imaging, *Mol Imaging Biol*, vol. 9, 2007, pp. 78-82.
[6] J. Sijbers, A. J. den Dekker, E. Raman, et al., Parameter estimation from magnitude MR images, *Int J Imaging Sys Techn*, Vol. 10, 1999, p. 109114.
[7] R. K.-S Kwan,A. C. Evans,G. B. Pike, MRI simulation-based evaluation of image-processing and classification methods, *IEEE Tr Med Imaging*, vol. 18, 1999, pp. 085 - 1097.
[8] D. J. Lomas, Technical developments in bowel MRI, *Eur Rad*, vol. 13, 2003, pp. 1058-1071.
[9] S. Mirzaei, M. Guerchaft, C. Bonnier, et al., Use of segmented CT transmission map to avoid metal artifacts in PET images by a PET-CT device, *BMC Nuc Med*, vol. 5, 2005, pp. 1-7.
[10] M. Styner, C. Brechbuhler, G. Szckely, et al., Parametric estimate of intensity inhomogeneities applied to MRI, *IEEE Tr Med Imaging*, vol. 19, 2000, pp. 153-165.
[11] J. E. Gentle, Computational Statistics, *Springer*, 2009.
[12] N. Zsoter, P. Bandi, I. Garai, et al., Hextuple registration of interim and follow-up PET-CT images for the accurate tracking of patient recovery after therapy, *Conf Proc IEEE Eng Med Biol Soc*, 2011, pp. 2630-2633.
[13] J. P. W. Pluim, J. B. A. Maintz, M. A. Viergever, et al., Mutual-information-based registration of medical images: a survey, *IEEE Transactions on Medical Imaging*, vol. 22, 2003, pp. 986 - 1004.
[14] J.L Bernon, V Boudousqa, J.F Rohmer, et al., A comparative study of Powell's and Downhill Simplex algorithms for a fast multimodal surface matching in brain imaging, *Comp Med Img Graph*, vol. 25, 2001, pp. 287-297.
[15] L. Shapiro, G. Stockman, Computer Vision, *Prentice Hall*, 2002, pp. 6973.
[16] M. Magdics, L. Szirmay-Kalos, B. Toth, et al., Performance evaluation of scatter modeling of the GPU-based Tera-Tomo 3D PET reconstruction, *Conf Proc IEEE NSS-MIC*, 2011, pp. 4086-4088.
[17] V. Daniel, MRI of bone metastases: the choice of the sequence, *Cancer Imaging*, vol. 4, 2004, pp. 30-35.